Anomalous thermal radiation due to the chiral magnetic effect in Weyl semimetals

Satoru Konabe *

Department of Chemical Science and Technology, Hosei University, Tokyo 184-8584, Japan

(Received 10 November 2023; accepted 8 February 2024; published 28 February 2024)

Thermal radiation, universally governed by Planck's law for objects at nonzero temperatures, is known to deviate in the near-field regime. In the present paper, we uncover a distinctive thermal radiation behavior in Weyl semimetals, challenging the established principles of Planck's law, even in the far-field regime. The chiral anomaly inherent to these materials gives rise to unique electromagnetic phenomena—namely, the anomalous Hall effect, which cause a breakdown of Kirchhoff's law, and the chiral magnetic effect. We theoretically demonstrate that the latter effect can induce negative emissivity at low-frequency ranges, suggesting an energy transfer from cooler to warmer bodies. This unexpected emissivity opens up novel approaches for thermal energy management using Weyl semimetals, with significant potential for future technological innovations.

DOI: 10.1103/PhysRevB.109.085145

I. INTRODUCTION

Thermal radiation is a ubiquitous physical phenomenon exhibited by all objects of finite temperature. This phenomenon is universally governed by Planck's law [1], which dictates that a blackbody's thermal radiation emission follows a specific broadband distribution solely dependent on the object's temperature. Significantly, Planck's law delineates an upper limit for the spectral distribution of the emitted thermal radiation. Nevertheless, there are scenarios where Planck's law does not hold. One notable example is the near-field radiation. Since Planck's law is rooted in the premise that all dimensions of the object surpass the thermal wavelength, the law fails to account for radiative heat transfers between objects with separations less than the thermal wavelength [2–4]. In such near-field conditions, evanescent waves, which Planck's law overlooks, dominate the radiative heat transfer, allowing the blackbody limit to be surpassed when objects are brought close enough. Moreover, the law's reliability may also be questioned in far-field scenarios where it overlooks factors like diffraction. This oversight leads to expected deviations for objects with dimensions smaller than the thermal wavelength. Notably, nanophotonic structures, with their subwavelength-scale features, demonstrate thermal radiation behaviors that depart from those of standard thermal emitters [5]. Proposals have even suggested that far-field thermal radiation from an object could surpass that of a blackbody [6,7], although these ideas have been challenged by later research [8,9]. In a different vein, emerging quantum materials such as Weyl semimetals are anticipated to display distinctive thermal radiation profiles due to their unique electromagnetic properties [10,11], which stand in contrast to those of conventional materials.

Weyl semimetals are three-dimensional quantum materials with unique topological properties. These materials host low-energy states characterized by Weyl fermions of both right- and left-handedness at specific points within the Brillouin zone [12,13]. In such systems, the presence of a chiral anomaly can interrupt the conservation of chiral current. This disruption has the potential to give rise to distinctive transport phenomena, including the anomalous Hall effect [14,15] and the chiral magnetic effect [16–18]. These phenomena are characterized by anomalous Hall and chiral magnetic currents, which are respectively given as

$$\boldsymbol{j}_{\mathrm{A}} = \frac{e^2}{2\pi^2\hbar}\boldsymbol{b}\times\boldsymbol{E}, \tag{1}$$

and

$$\boldsymbol{j}_{\mathrm{C}} = \frac{e^2}{2\pi^2\hbar^2}\mu_5\boldsymbol{B}. \tag{2}$$

Here, as shown in Fig. 1, $2\boldsymbol{b}$ is the distance between the two Weyl points and $2\mu_5 \equiv \mu_R - \mu_L$ is the chiral chemical potential that is defined as the difference between the chemical potentials of the right- and left-handed Weyl fermions. The chiral magnetic effect is shown to occur only in a nonequilibrium state where the chiral chemical potential μ_5 is nonzero [17,18]. When electric and magnetic fields are applied, the chiral anomaly induces an axial charge difference between right- and left-handed Weyl fermions [19–21], leading to a nonzero chiral chemical potential.

Theoretical studies have already established the significant influence of the anomalous Hall effect on thermal radiation, leading to a violation of Kirchhoff's law [22,23]—one of the foundational principles of thermal radiation alongside Planck's law. This violation manifests as nonreciprocal thermal radiation [24,25] and the generation of highly pure circularly polarized thermal radiation [26,27].

However, the implications of the chiral magnetic effect on thermal radiation remain unexplored. Recently, Nishida found that the chiral instability [28] due to the chiral magnetic effect causes the circular polarized reflectance of Weyl semimetals to exceed unity [29]. Given the close relationship between a

*konabe@hosei.ac.jp

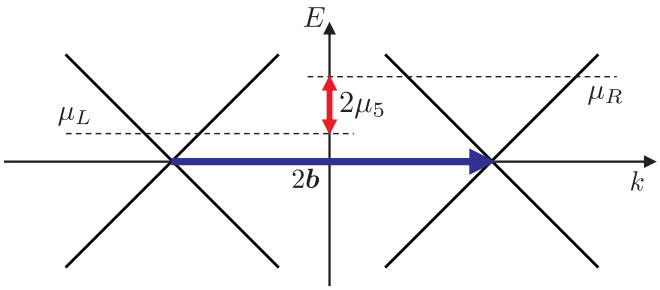

FIG. 1. Energy dispersion of the Weyl semimetals and definition of $\boldsymbol{b}$ and μ_5.

material's optical and thermal radiation properties, the chiral magnetic effect suggests to induce anomalous behaviors in thermal radiation as well. This study addresses the gap by investigating the chiral magnetic effect's influence on thermal radiation. We report the theoretical discovery that emissivity can turn negative at low frequencies, leading to the energy transfer from cooler to warmer bodies.

II. THEORY

We consider that the system consists of a Weyl semimetal in $z < 0$ and the vacuum in $z > 0$ and assume that the Weyl semimetal is sufficiently thick that electromagnetic waves do not penetrate the Weyl semimetal.

A. Thermal radiation and emissivity

The thermal radiation propagates in the direction defined by the angles (θ, ϕ), where θ is the angle with the z-axis and ϕ is the angle made by the in-plane component of the radiation direction with the x-axis (Fig. 2). Thermal radiation per unit area emitted by the object is given by

$$H_\eta = \int d\omega \int d\Omega\, \eta(\theta, \phi) I_b(\omega, T) \cos\theta, \tag{3}$$

where ω is the frequency, Ω is the solid angle, $\eta(\theta, \phi)$ is the dimensionless emissivity, and $I_b(\omega, T) = [\omega^2/(4\pi^3 c^2)]\{(\hbar\omega)/[\exp(\hbar\omega/k_B T) - 1]\}$ is the blackbody radiance at temperature T. Emissivity $\eta(\theta, \phi)$ expresses the material-specific property of thermal radiation and usually takes the value $0 < \eta(\theta, \phi) < 1$. For normal materials where Kirchhoff's law is satisfied, the absorptivity is equal to the emissivity and is typically used in (3) instead

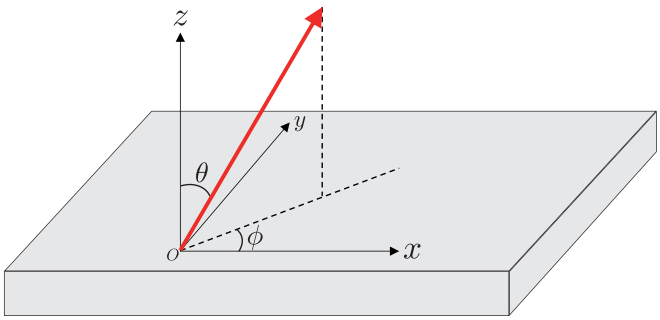

FIG. 2. Definition of the thermal radiation direction.

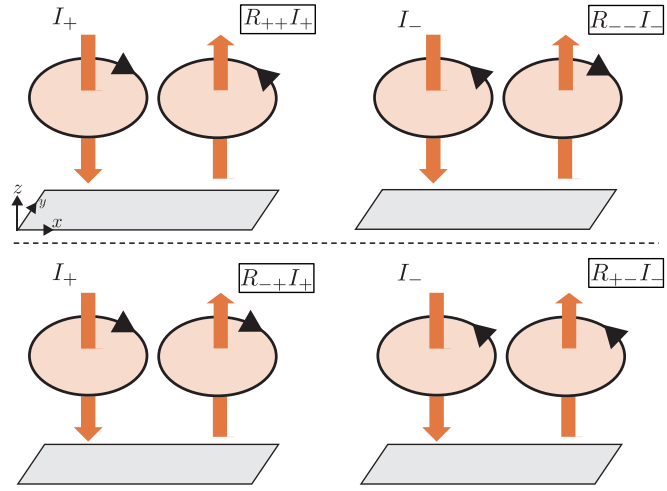

FIG. 3. Polarization conventions of thermal radiation from the planar surface of a Weyl semimetal. $I_\pm$ is the polarized blackbody radiance.

of emissivity. The Weyl semimetals are nonreciprocal materials, however, therefore, Kirchhoff's law cannot be used. Fluctuational electrodynamics [30] are thus employed to directly derive the emissivity, or the thermal radiation formula [31]. Accordingly, it is shown that for the circular polarized thermal radiation of interest here, the dimensionless emissivity $\eta(\theta, \phi)$ is the sum of the left circular polarized emissivity η_+ and the right circular-polarized emissivity η_-: $\eta(\theta, \phi) = [\eta_+(\theta, \phi) + \eta_-(\theta, \phi)]/2$. Here, η_+ and η_- are expressed by the reflectance [26]

$$\eta_+(\theta, \phi) = 1 - R_{++}(\theta, \phi + \pi) - R_{+-}(\theta, \phi + \pi), \tag{4}$$

$$\eta_-(\theta, \phi) = 1 - R_{-+}(\theta, \phi + \pi) - R_{--}(\theta, \phi + \pi), \tag{5}$$

where R_{ij} $(i, j = +, -)$ is the reflectance of i circular polarized light for j circular polarized incident waves, which is derived below. The definition of the polarization is given in Fig. 3.

B. Reflectance

The following Maxwell equation is solved with the suitable boundary condition to obtain reflectance at the surface $z = 0$ of the Weyl semimetal

$$\nabla \times \boldsymbol{B}(\boldsymbol{r}, t) - \frac{1}{v^2} \frac{\partial \boldsymbol{E}(\boldsymbol{r}, t)}{\partial t} = \mu \boldsymbol{j}(\boldsymbol{r}, t), \tag{6}$$

where v and $\mu = \mu_r \mu_0$ are the light velocity and the permeability in the Weyl semimetal, respectively.

The electric current in Weyl semimetals is derived using the consistent chiral kinetic theory with the relaxation-time approximation [32,33], which is given as

$$\boldsymbol{j}(\boldsymbol{r}, t) = \sigma_E \boldsymbol{E}(\boldsymbol{r}, t) + \sigma_M \boldsymbol{B}(\boldsymbol{r}, t) + \sigma_H \hat{\boldsymbol{b}} \times \boldsymbol{E}(\boldsymbol{r}, t), \tag{7}$$

where $\hat{\boldsymbol{b}}$ is the unit vector of $\boldsymbol{b}$. Here, we assume that $\boldsymbol{b}$ is oriented along the z-axis. The terms with σ_E, σ_M, and σ_H represent the ohmic conduction, the chiral magnetic effect, and the anomalous Hall effect, respectively. For sufficiently slow external fields with $|\omega|, v_F|\boldsymbol{k}| \ll 1/\tau \ll k_B T/\hbar, \mu_R/\hbar, \mu_L/\hbar,$

where v_F is the Fermi velocity and τ is the intravalley relaxation time, the conductivities are provided by $\sigma_E = [(e^2\tau)/(6\pi^2\hbar^3 v_F)][(2\pi^2(k_BT)^2)/3 + \mu_L^2 + \mu_R^2]$, $\sigma_M = e^2\mu_5/(2\pi^2\hbar^2)$, and $\sigma_H = e^2|\boldsymbol{b}|/(2\pi^2\hbar)$ [29,33].

When an electromagnetic wave is incident from the vacuum side ($z > 0$) at an angle (θ, ϕ), as defined in Fig. 2, the incident wave is expressed as

$$\boldsymbol{E}^i(\boldsymbol{r}, t) = \left(E_s\boldsymbol{e}_s^i + E_p\boldsymbol{e}_p^i\right)e^{i(k_{t0}\cos\phi x + k_{t0}\sin\phi y - k_{z0}z) - i\omega t}. \quad (8)$$

Here, we use the basis of s- and p-waves:

$$\boldsymbol{e}_s^i = (\sin\phi, -\cos\phi, 0), \quad (9)$$

$$\boldsymbol{e}_p^i = \frac{(k_{z0}\cos\phi, k_{z0}\sin\phi, k_{t0})}{\sqrt{k_{t0}^2 + k_{z0}^2}}, \quad (10)$$

where $k_{t0}(\omega) \equiv k_0\sin\theta = \frac{\omega}{c}\sin\theta$ and $k_{z0}(\omega) \equiv k_0\cos\theta = \frac{\omega}{c}\cos\theta$, with $k_0 = \omega/c$. The reflected wave is expressed as

$$\boldsymbol{E}^r(\boldsymbol{r}, t) = \left(E_s r_{ss}\boldsymbol{e}_s^r + E_p r_{pp}\boldsymbol{e}_p^r + E_s r_{ps}\boldsymbol{e}_p^r + E_p r_{sp}\boldsymbol{e}_s^r\right) \times e^{i(k_{t0}\cos\phi x + k_{t0}\sin\phi y + k_{z0}z) - i\omega t}, \quad (11)$$

where $r_{ij}(i, j = s, p)$ denotes the Fresnel reflection coefficient when an incident wave with j-polarization is reflected with i-polarization. The basis of the reflected wave is given as

$$\boldsymbol{e}_s^r = (\sin\phi, -\cos\phi, 0), \quad (12)$$

$$\boldsymbol{e}_p^r = \frac{(-k_{z0}\cos\phi, -k_{z0}\sin\phi, k_{t0})}{\sqrt{k_{t0}^2 + k_{z0}^2}}. \quad (13)$$

On the other hand, the transmission wave to the Weyl semimetal region ($z < 0$) is given by

$$\boldsymbol{E}^t(\boldsymbol{r}, t) = \left(E_s t_{ss}\boldsymbol{e}_s^t + E_p t_{pp}\boldsymbol{e}_p^t + E_s t_{ps}\boldsymbol{e}_p^t + E_p t_{sp}\boldsymbol{e}_s^t\right) \times e^{i(k_{t0}\cos\phi x + k_{t0}\sin\phi y - k_z z) - i\omega t}, \quad (14)$$

where $t_{ij}(i, j = s, p)$ denotes the Fresnel transmission coefficient for an incident wave with j-polarization transmitted with i-polarization. The basis of the transmission wave is given as

$$\boldsymbol{e}_s^t = (\sin\phi, -\cos\phi, 0), \quad (15)$$

$$\boldsymbol{e}_p^t = \frac{(k_z\cos\phi, k_z\sin\phi, k_{t0})}{\sqrt{k_{t0}^2 + k_z^2}}. \quad (16)$$

The dispersion relation $k_z(\omega)$ of the electromagnetic wave in the Weyl semimetals can be obtained by substituting the transmitted wave (14) into the Maxwell equation (6) and solving the characteristic equation obtained as the determinant of the coefficient matrix of E_s^t and E_p^t being zero. This yields four distinct solutions: two manifest as traveling waves that propagate in the $-z$ direction, while the remaining two move in the z direction. Among these, the pair of solutions $k_z^{(i)}$ $(i = 1, 2)$ that exhibit a decay for $z \to -\infty$ within the Weyl semimetal is selected. The characteristic equation can be solved analytically in the limit of $(\theta, \phi) = (0, 0)$ [29], and for $\omega > 0$:

$$k_z^{(i)}(\omega) = \pm\frac{\mu\sigma_M}{2} - \sqrt{\left(\frac{\mu\sigma_M}{2}\right)^2 + i\mu\sigma_E\omega \mp \mu\sigma_H\omega + \left(\frac{\omega}{v}\right)^2}, \quad (17)$$

where $i = 1, 2$ corresponds to $\pm$ representing the two solutions that satisfy the boundary condition at $z \to -\infty$.

The Fresnel coefficients can be obtained using the boundary condition of the electromagnetic field at $z = 0$: $\boldsymbol{E}(\boldsymbol{r}, t)|_{z\to-0} = \boldsymbol{E}(\boldsymbol{r}, t)|_{z\to+0}$ and $\boldsymbol{B}(\boldsymbol{r}, t)|_{z\to-0}/\mu = \boldsymbol{B}(\boldsymbol{r}, t)|_{z\to+0}/\mu_0$. Hereafter, we set $\mu = \mu_0$ ($\mu_r = 1$). The substitution of (8), (11), and (14) into these conditions gives the Fresnel reflection coefficient r_{ij} and Fresnel transmission coefficient t_{ij}. Using the Fresnel reflection coefficients r_{ij} for the s and p waves obtained, the circular polarized reflectance can be expressed as

$$R_{++}(\theta, \phi) = \frac{|(r_{ss} + r_{pp}) + i(r_{sp} - r_{ps})|^2}{4}, \quad (18)$$

$$R_{--}(\theta, \phi) = \frac{|(r_{ss} + r_{pp}) - i(r_{sp} - r_{ps})|^2}{4}, \quad (19)$$

$$R_{-+}(\theta, \phi) = \frac{|(r_{ss} - r_{pp}) + i(r_{sp} + r_{ps})|^2}{4}, \quad (20)$$

$$R_{+-}(\theta, \phi) = \frac{|(r_{ss} - r_{pp}) - i(r_{sp} + r_{ps})|^2}{4}. \quad (21)$$

III. RESULTS

A. Anomalous reflectance

To capture the essence of the anomalous reflection and thermal radiation, R_{ij} and η are first analyzed in the zero frequency limit at $(\theta, \phi) = (0, 0)$ by deriving the analytical expressions.

The reflectances in the zero frequency limit at $(\theta, \phi) = (0, 0)$ are analytically derived as

$$\lim_{\omega\to0} R_{++}(0, 0) = \begin{cases} \dfrac{4\sigma_H^2\sigma_M^2}{\left(\sigma_E^2 + \sigma_H^2\right)[(c\sigma_H + \sigma_M)^2 + (c\sigma_E)^2]} & (\sigma_M > 0), \\ 0 \quad (\sigma_M < 0), \end{cases} \quad (22)$$

$$\lim_{\omega\to0} R_{--}(0, 0) = \begin{cases} 0 \quad (\sigma_M > 0), \\ \dfrac{4\sigma_H^2\sigma_M^2}{\left(\sigma_E^2 + \sigma_H^2\right)[(c\sigma_H + \sigma_M)^2 + (c\sigma_E)^2]} & (\sigma_M < 0), \end{cases} \quad (23)$$

$$\lim_{\omega\to0} R_{-+}(0, 0) = \begin{cases} \dfrac{(c\sigma_H - \sigma_M)^2 + (c\sigma_E)^2}{(c\sigma_H + \sigma_M)^2 + (c\sigma_E)^2} & (\sigma_M > 0), \\ 1 \quad (\sigma_M < 0), \end{cases} \quad (24)$$

$$\lim_{\omega\to0} R_{+-}(0, 0) = \begin{cases} 1 \quad (\sigma_M > 0), \\ \dfrac{(c\sigma_H - \sigma_M)^2 + (c\sigma_E)^2}{(c\sigma_H + \sigma_M)^2 + (c\sigma_E)^2} & (\sigma_M < 0). \end{cases} \quad (25)$$

Two interesting features are noted in these expressions. The first is that the interconversion reflectances R_{++} and R_{--} can manifest finite values for $\sigma_M > 0$ and $\sigma_M < 0$, respectively.

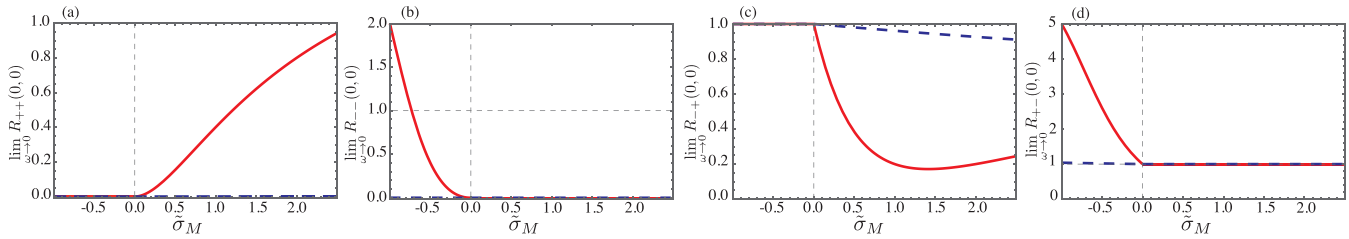

FIG. 4. (a) $\lim_{\omega\to 0} R_{++}(0,0)$, (b) $\lim_{\omega\to 0} R_{--}(0,0)$, (c) $\lim_{\omega\to 0} R_{-+}(0,0)$, and (d) $\lim_{\omega\to 0} R_{+-}(0,0)$ as functions of $\tilde{\sigma_M}$. Solid and dashed lines represent the cases of $\tilde{\sigma}_E = 1$ and $\tilde{\sigma}_E = 10$, respectively.

This is attributed to the chiral magnetic effects, as indicated by σ_M that appears in the numerators of Eqs. (22) and (23) for R_{++} and R_{--}. Such behavior is expected from the term that represents the chiral magnetic effect within Maxwell's equations. The electric field is expressed as the superposition of the two plane waves $\boldsymbol{E}_1 e^{i(\boldsymbol{k}^{(1)}\cdot\boldsymbol{r}-\omega t)} + \boldsymbol{E}_2 e^{i(\boldsymbol{k}^{(2)}\cdot\boldsymbol{r}-\omega t)}$; therefore, the term that represents the chiral magnetic effect in the Maxwell equation (6) becomes $i\mu\sigma_M(\boldsymbol{k}^{(1)}\times\boldsymbol{E}_1 + \boldsymbol{k}^{(2)}\times\boldsymbol{E}_2)$. This certainly shows that polarization mixing in the electric fields $\boldsymbol{E}_1$ and $\boldsymbol{E}_2$ may occur, depending on the form of $\boldsymbol{k}^{(i)}$.

The second feature is that R_{+-} exceeds unity for any $\sigma_M < 0$ [29], while R_{--} also exceeds unity below a specific value of σ_M that is given as

$$\sigma_M = -\frac{c\left(\sigma_E^2+\sigma_H^2\right)\left(-\sigma_H+\sqrt{4\sigma_H^2-\sigma_E^2}\right)}{3\sigma_H^2-\sigma_E^2} \tag{26}$$

in regions where σ_M is negative. The physical origin of the anomalous reflectance for $\sigma_M < 0$ at $(\theta,\phi) = (0,0)$ is clarified in Ref. [29]. The dispersion relation $k_z(\omega)$ given by Eq. (17) has the negative real part for the finite range of ω for $\sigma_M < 0$. For such frequencies, the electromagnetic wave grows exponentially toward the direction of its propagation as a result of the dynamical instability of the magnetic field, referred to as the chiral magnetic instability [28,29,33]. Accordingly, the electromagnetic wave at $z < 0$ in the Weyl semimetal anomalously grows toward the surface, which leads to the reflectance that exceeds unity. We note that the chiral magnetic instability occurs at nonequilibrium with chirality imbalance and the amplification of reflected wave decreases the chirality imbalance [29].

The anomalous reflection is expected for $\sigma_E \leqslant \sigma_H \approx |\sigma_M|/c$ [29] although the actual values of the current situation satisfies $\sigma_M/c \ll \sigma_H \ll \sigma_E$. To demonstrate the impact of these different conditions, the reflectances are plotted by rewriting them in terms of the dimensionless conductivities $\tilde{\sigma}_E \equiv \sigma_E/\sigma_H$ and $\tilde{\sigma}_M \equiv \sigma_M/c\sigma_H$. Figure 4 shows the reflectances for $\tilde{\sigma}_E = 1$ and $\tilde{\sigma}_E = 10$ as a function of $\tilde{\sigma}_M$ ($-1 \leqslant \tilde{\sigma}_M \leqslant 2.5$). In regions where $\tilde{\sigma}_M$ is negative, both R_{--} and R_{+-} are well above unity for $\tilde{\sigma}_E = 1$, while R_{--} is less than unity and R_{+-} is slightly above unity for $\tilde{\sigma}_E = 10$.

B. Anomalous emissivity

Emissivity is determined by reflectance, as indicated by Eqs. (4) and (5); therefore, anomalous behavior of reflectance is expected to have a significant influence on emissivity. To demonstrate how anomalous reflectance affects thermal radiation, an analytical expression for emissivity is derived, which holds for both $\sigma_M >$ and $\sigma_M < 0$:

$$\lim_{\omega\to 0}\eta(0,0) = \frac{2\sigma_H\sigma_M\left[c\left(\sigma_E^2+\sigma_H^2\right)-\sigma_H\sigma_M\right]}{\left(\sigma_E^2+\sigma_H^2\right)\left[(c\sigma_H+\sigma_M)^2+(c\sigma_E)^2\right]}. \tag{27}$$

For far-field thermal radiation, emissivity takes the value $0 < \eta < 1$. However, Eq. (27) clearly shows that emissivity assumes negative values when $\sigma_M < 0$. This is ascribed to the anomalous reflectance due to the chiral magnetic instability.

Furthermore, it is noted that emissivity can be negative, even for $\sigma_M > 0$, when $\sigma_H\sigma_M > c(\sigma_E^2+\sigma_H^2)$. In this case, the chiral magnetic instability is irrelevant to the negative emissivity since $\sigma_M > 0$; rather, the negative emissivity is due to the interconversion reflectance R_{++} being finite due to the chiral magnetic effect.

Similarly to reflectance, the conductivity dependence of emissivity is examined by rewriting Eq. (27) using the dimensionless conductivities. Figure 5 shows emissivity for $\tilde{\sigma}_E = 1$ and $\tilde{\sigma}_E = 10$ as a function of $\tilde{\sigma}_M$. As anticipated, for $\tilde{\sigma}_E = 1$, the emissivity becomes negative when $\tilde{\sigma}_M <$ or $\tilde{\sigma}_M > \tilde{\sigma}_E^2 + 1(= 2)$. On the other hand, this anomalous behavior is largely mitigated when $\tilde{\sigma}_E = 10$.

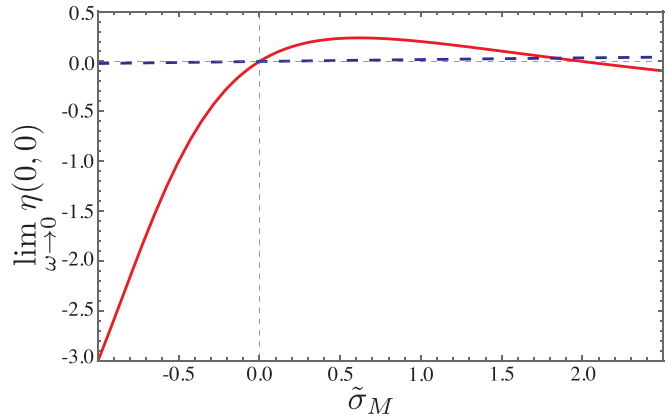

FIG. 5. $\lim_{\omega\to 0}\eta(0,0)$ as a function of $\tilde{\sigma_M}$. Solid and dashed lines represent the cases of $\tilde{\sigma}_E = 1$ and $\tilde{\sigma}_E = 10$, respectively.

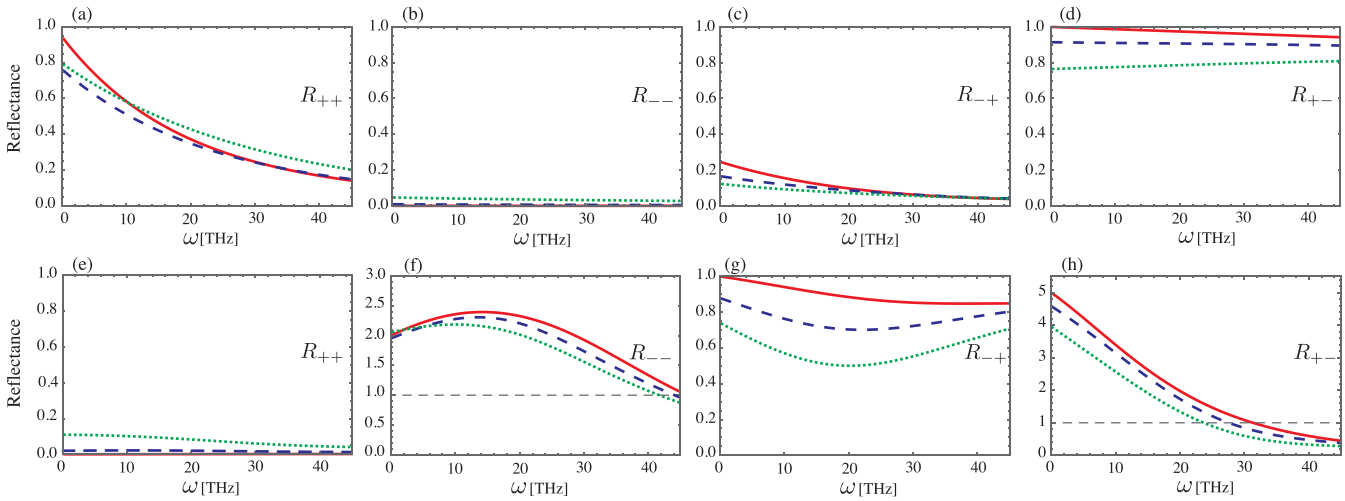

FIG. 6. Frequency dependence of circular polarized reflectance (a) [(e)] $R_{++}(\theta, \phi)$, (b) [(f)] $R_{--}(\theta, \phi)$, (c) [(g)] $R_{-+}(\theta, \phi)$, and (d) [(h)] $R_{+-}(\theta, \phi)$ for $\sigma_M > 0$ ($\sigma_M < 0$). Solid, dashed, and dotted lines represent the cases of incident angles 0, $\pi/6$, and $\pi/4$, respectively. The parameters are set to $v = c/6$, $\sigma_H = 10^4\ \Omega^{-1}\ \mathrm{m}^{-1}$, $\sigma_E = \sigma_H$, and $\sigma_M = 2.5 \times c\sigma_H$ ($\sigma_M = -c\sigma_H$) for [(a)–(d)] [(e)–(h)].

C. Incident angle and frequency dependence

To further characterize the reflectance and emissivity in detail, numerical results for (θ, ϕ) and ω dependence are then presented.

Following Ref. [29], the numerical calculations are performed at the level of order estimation under the condition that satisfies $\sigma_E \leqslant \sigma_H \approx |\sigma_M|/c$, where anomalous behavior is most pronounced, although it is an unrealistic condition for now. The anomalous Hall conductivity is first set to $\sigma_H \simeq 10^4\ \Omega^{-1} m^{-1} \equiv \sigma_{H0}$, which corresponds to $|2\boldsymbol{b}| = 10^9\ \mathrm{m}^{-1}$ [34,35]. To maximize the reflectance at zero frequency, $\sigma_M = 2.5 \times c\sigma_{H0}/\mu_r$ for $\sigma_M > 0$ and $\sigma_M = -c\sigma_{H0}/\mu_r$ for $\sigma_M < 0$ are then selected. Finally, $\sigma_E = \sigma_{H0}$ is set so that the anomalous behavior appears.

Figure 6 plots the frequency dependence of the reflectance R_{ij} of circular polarized light for various incident angles of $\theta = 0, \pi/6$, and $\pi/4$ with $\phi = 0$. The case of $\sigma_M > 0$ shown in Figs. 6(a) to 6(d) is examined first. As discussed in the analysis of Eqs. (22) to (25), the most important point is that the chiral magnetic effect causes the interconversion reflection with finite values of R_{++} for a broad range of frequency. The case of $\sigma_M < 0$ shown in Figs. 6(e) to 6(h) is considered next. When the incident wave is the left circular polarized wave shown in Figs. 6(e) and 6(g), the reflectance does not exceed unity at any frequency. On the other hand, in the case of the right circular polarized incident wave shown in Figs. 6(f) and 6(h), the reflectance exceeds unity when the frequency is smaller than a certain value due to the chiral magnetic instability. As demonstrated in Eqs. (23) and (25), the reflectance exceeds unity even for polarization interconversion reflectance such as R_{--} as well as R_{+-}.

Figure 7 plots the frequency dependence of the total emissivity, the left circular polarized emissivity, and the right circular polarized emissivity for different incident angles of $\theta = 0$, $\pi/6$, and $\pi/4$ with $\phi = 0$. The case for $\sigma_M > 0$ shown in Figs. 7(a) to 7(c) is examined first. The crucial point in this case is that, as shown in Fig. 7(b), the circular polarized emissivity η_+ becomes negative in the low-frequency region. On the other hand, η_- shown in Fig. 7(c) is positive for any frequency. The difference arises because the interconversion reflection occurs only for the incident wave with the left circular polarization for $\sigma_M > 0$. As a result, for the present parameters where $\sigma_H\sigma_M > c(\sigma_E^2 + \sigma_H^2)$ holds, the total emissivity at $(\theta, \phi) = (0, 0)$ shown in Fig. 7(a) can be negative as discussed in the case of the zero frequency limit (see Fig. 5). The case for $\sigma_M < 0$ shown in Figs. 7(d) to 7(f) is considered next. Both circular polarized emissivities η_+ and η_- shown in Figs. 7(e) and 7(f) take a negative value when the frequency is smaller than a certain value because R_{+-} (R_{--}) in η_+ (η_-) exceeds unity due to the chiral magnetic instability. Therefore, the total emissivity shown in Fig. 7(d) also becomes negative in the low-frequency region.

As observed from the incident angle (θ) dependence, vertical incidence shows the most pronounced anomalous reflection. The anomalous behavior of emissivity is thus also more pronounced for smaller incident angles.

IV. DISCUSSION

Now consider the physical consequence of a negative emissivity. Spectral heat flux from an object at temperature T into the environment (vacuum) at temperature T_e ($T > T_e$) is given by

$$dH_\eta = \eta(\theta, \phi)[I_b(\omega, T) - I_b(\omega, T_e)] \cos\theta d\omega d\Omega. \quad (28)$$

The total thermal radiation, as described in Eq. (3), is obtained by integrating Eq. (28) over all angles and frequencies, with the environmental temperature, T_e, set to zero. For cases where the emissivity is positive [$\eta(\theta, \phi) > 0$], Eq. (28) indicates that $dH_\eta > 0$, signifying that the spectral heat flux is directed from the object to the environment. Conversely, when the emissivity is negative ($\eta(\theta, \phi) < 0$), Eq. (28) leads to $dH_\eta < 0$, implying that the spectral heat flux may flow from the environment to the object. Therefore, when the

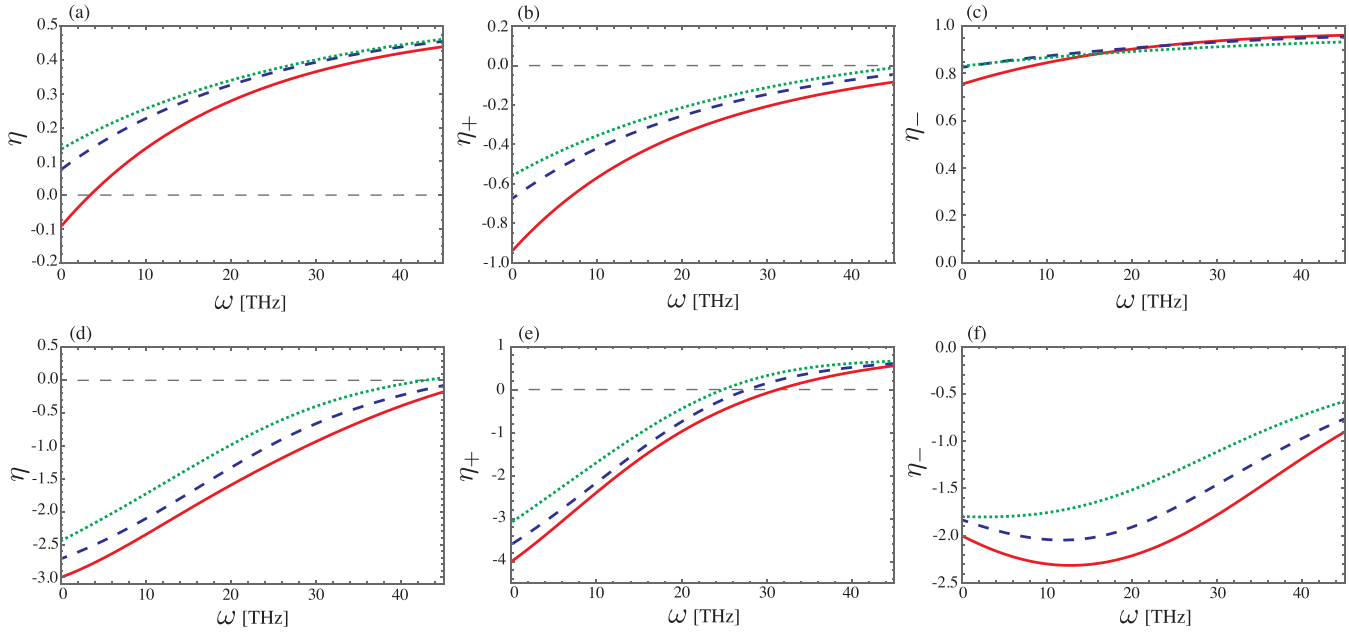

FIG. 7. Frequency dependence of (a) [(d)] $\eta(\theta, \phi)$, (b) [(e)] $\eta_+(\theta, \phi)$, and (c) [(f)] $\eta_-(\theta, \phi)$ for $\sigma_M > 0$ ($\sigma_M < 0$). Solid, dashed, and dotted lines represent the cases of incident angles 0, $\pi/6$, and $\pi/4$, respectively. The parameters are set to $v = c/6$, $\sigma_H = 10^4\ \Omega^{-1}\ \mathrm{m}^{-1}$, $\sigma_E = \sigma_H$, and $\sigma_M = 2.5 \times c\sigma_H$ ($\sigma_M = -c\sigma_H$) for [(a)–(c)] [(d)–(f)].

temperature of the Weyl semimetal is T and the temperature of the environment is T_e with $T > T_e$, energy flows from the environment with lower temperature to the Weyl semimetal with higher temperature. It should be noted that the observed behavior might appear to contravene the second law of thermodynamics if the system were in thermal equilibrium. However, this is not the case for a Weyl semimetal with a finite chiral chemical potential, i.e., $\mu_5 \neq 0$, as it inherently exists in a nonequilibrium state.

Furthermore, emissivity is negative only within a specific low-frequency region, whereas it turns positive at higher frequencies. Consequently, when considering thermal radiation integrated over frequency, the net effect should result in a positive emissivity, ensuring that overall thermal radiation still flows from hot to cold objects. This is corroborated by the result that the total emissivity, defined as H_η/H_b [with H_b representing black body radiation, obtained by setting $\eta = 1$ in Eq. (3)], remains positive, as demonstrated in Fig. 8. It has been theoretically shown that negative emissivity can occur in nonlinear materials, although the underlying mechanism is entirely different [36].

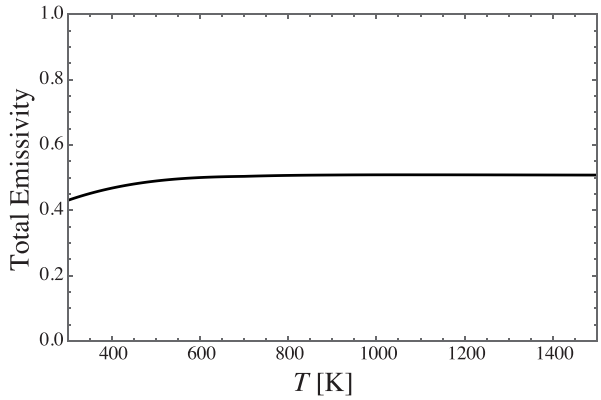

FIG. 8. Temperature dependence of the total emissivity integrated over all angles and frequencies.

V. SUMMARY

In summary, we conducted a theoretical exploration of the chiral magnetic effect on the thermal radiation properties of Weyl semimetals. This effect causes circularly polarized reflectance to exceed unity, indicating possible anomalies in emissivity. To investigate this, we analytically calculated the circularly polarized reflectance and emissivity at zero frequency and normal incidence and carried out numerical calculations at finite frequencies and various incident angles. A key discovery is that emissivity can become negative when chiral magnetic conductivity is negative—a sign of chiral magnetic instability. Additionally, we identified conditions where emissivity turns negative independently of such instability, attributed to interconversion reflection caused by the chiral magnetic effect. Negative emissivity suggests that energy could flow from colder to hotter regions. This distinct emissivity behavior opens up innovative ways to harness radiant thermal energy, presenting new possibilities for thermal engineering with Weyl semimetals.

ACKNOWLEDGMENTS

This work was supported, in part, by JSPS KAKENHI (Grants No. 20H05664, No. 22H00575, and No. 22K04912), JST CREST (Grant No. JPMJCR18I5), and the ZE Research Program, IAE (Grant No. ZE2023B-32).

[1] M. Planck, Ann. Phys. (Leipzig) **309**, 553 (1901).
[2] K. Joulain, J. P. Mulet, F. Marquier, R. Carminati, and J. J. Greffet, Surf. Sci. Rep. **57**, 59 (2005).
[3] S. Basu, Z. M. Zhang, and C. J. Fu, Int. J. Energy Res. **33**, 1203 (2009).
[4] B. Song, A. Fiorino, E. Meyhofer, and P. Reddy, AIP Adv. **5**, 053503 (2015).
[5] W. Li and S. Fan, Opt. Express **26**, 15995 (2018).
[6] I. S. Nefedov and L. A. Melnikov, Appl. Phys. Lett. **105**, 161902 (2014).
[7] S. I. Maslovski, C. R. Simovski, and S. A. Tretyakov, New J. Phys. **18**, 013034 (2016).
[8] S. A. Biehs and P. Ben-Abdallah, Phys. Rev. B **93**, 165405 (2016).
[9] J. J. Greffet, P. Bouchon, G. Brucoli, and F. Marquier, Phys. Rev. X **8**, 021008 (2018).
[10] N. P. Armitage, E. J. Mele, and A. Vishwanath, Rev. Mod. Phys. **90**, 015001 (2018).
[11] E. V. Gorbar, V. A. Miransky, I. A. Shovkovy, and P. O. Sukhachov, *Electronic Properties of Dirac and Weyl Semimetals* (World Scientific, Singapore, 2021).
[12] S. Murakami, New J. Phys. **9**, 356 (2007).
[13] X. Wan, A. M. Turner, A. Vishwanath, and S. Y. Savrasov, Phys. Rev. B **83**, 205101 (2011).
[14] K.-Y. Yang, Y.-M. Lu, and Y. Ran, Phys. Rev. B **84**, 075129 (2011).
[15] A. A. Burkov and L. Balents, Phys. Rev. Lett. **107**, 127205 (2011).
[16] K. Fukushima, D. E. Kharzeev, and H. J. Warringa, Phys. Rev. D **78**, 074033 (2008).
[17] M. M. Vazifeh and M. Franz, Phys. Rev. Lett. **111**, 027201 (2013).
[18] G. Başar, D. E. Kharzeev, and H.-U. Yee, Phys. Rev. B **89**, 035142 (2014).
[19] S. L. Adler, Phys. Rev. **177**, 2426 (1969).
[20] J. S. Bell and R. Jackiw, Nuov Cim. A **60**, 47 (1969).
[21] H. B. Nielsen and M. Ninomiya, Phys. Lett. B **130**, 389 (1983).
[22] G. Kirchhoff, Philos. Mag. Ser. 5 **20**, 1 (1860).
[23] L. Zhu and S. Fan, Phys. Rev. B **90**, 220301(R) (2014).
[24] B. Zhao, C. Guo, C. A. C. Garcia, P. Narang, and S. Fan, Nano Lett. **20**, 1923 (2020).
[25] Y. Tsurimaki, X. Qian, S. Pajovic, F. Han, M. Li, and G. Chen, Phys. Rev. B **101**, 165426 (2020).
[26] C. Khandekar, F. Khosravi, Z. Li, and Z. Jacob, New J. Phys. **22**, 123005 (2020).
[27] Y. Wang, C. Khandekar, X. Gao, T. Li, D. Jiao, and Z. Jacob, Opt. Mater. Express **11**, 3880 (2021).
[28] Y. Akamatsu and N. Yamamoto, Phys. Rev. D **90**, 125031 (2014).
[29] Y. Nishida, Phys. Rev. Lett. **130**, 096903 (2023).
[30] S. M. Rytov, Y. A. Kravtsov, and V. I. Tatarskii, *Principles of Statistical Radiophysics* (Springer-Verlag, Berlin, 1989), Vol. 3.
[31] M. Krüger, G. Bimonte, T. Emig, and M. Kardar, Phys. Rev. B **86**, 115423 (2012).
[32] E. V. Gorbar, V. A. Miransky, I. A. Shovkovy, and P. O. Sukhachov, Phys. Rev. Lett. **118**, 127601 (2017).
[33] T. Amitani and Y. Nishida, Phys. Rev. B **107**, 014302 (2023).
[34] S.-Y. Xu, I. Belopolski, N. Alidoust, M. Neupane, and G. Bian, Science **349**, 613 (2015).
[35] C.-L. Zhang, S.-Y. Xu, I. Belopolski, Z. Yuan, Z. Lin, B. Tong, G. Bian, N. Alidoust, C.-C. Lee, S.-M. Huang, T.-R. Chang, G. Chang, C.-H. Hsu, H.-T. Jeng, M. Neupane, D. S. Sanchez, H. Zheng, J. Wang, H. Lin, C. Zhang *et al.*, Nat. Commun. **7**, 10735 (2016).
[36] H. Soo and M. Krüger, Phys. Rev. B **97**, 045412 (2018).